Development of a Sustainable Heterogeneous Catalyst Based on an Open-Cell Glass Foam Support: Application in Gas-Phase Ozone Decomposition

Antoine Lejeune, Audrey Cabrol, Ronan Lebullenger, Audrey Denicourt-Nowicki, Alain Roucoux, Anthony Szymczyk, Annabelle Couvert, Pierre-Francois Biard

Development of a sustainable heterogeneous catalyst based on an open-cell glass foam support: application in gas-phase ozone decomposition

Antoine Lejeune †*, Audrey Cabrol †, Ronan Lebullenger ‡, Audrey Denicourt-Nowicki ‡, Alain Roucoux ‡, Anthony Szymczyk ‡, Annabelle Couvert ‡, Pierre-François Biard ‡

† SATT Ouest Valorisation, 14C Rue du Patis Tatelin, 35700 Rennes, France

‡ Univ Rennes, Ecole Nationale Supérieure de Chimie de Rennes, CNRS, ISCR (Institut des Sciences Chimiques de Rennes) - UMR 6226, F-35000, Rennes, France

*Corresponding author: anlejeun@gmail.com

Keywords

glass foam, ruthenium nanoparticles, catalyst, ozone removal, fixed bed

Abstract

Heterogeneous catalysts were synthesized with a glass foam support mainly composed of recycled glass and impregnated with zerovalent ruthenium nanoparticles (aiming to 0.1 wt.% ruthenium). Different glass foams were developed, playing on the nature and quantity of foaming/doping agents as well as the operating conditions (heat temperature and time of heating). They were characterized in terms of open porosity, pore diameter, wettability and pressure drops. High open porosity can be achieved (between 73% and 92%) with mean pore diameter up to 0.55 mm, resulting in the lowest pressure drops measured among all glass foams. The deposit of zerovalent ruthenium nanoparticles was confirmed by TEM images and changes in surface charge showed by zeta potential determination. Finally, the removal of ozone from air at room temperature and inlet concentration of 9 $g.Nm^{-3}$ was performed to prove the catalyst activity. Up to 52% of ozone decomposition was achieved in less than 13 seconds of residence time. The activity did not seem to be linked with the characteristics (open porosity and mean pore size) of the glass foams but it was shown that the external mass transfer was still limiting the process performances in the range of superficial gas velocity tested (4 $mm.s^{-1}$ to 11 $mm.s^{-1}$).

Graphical abstract

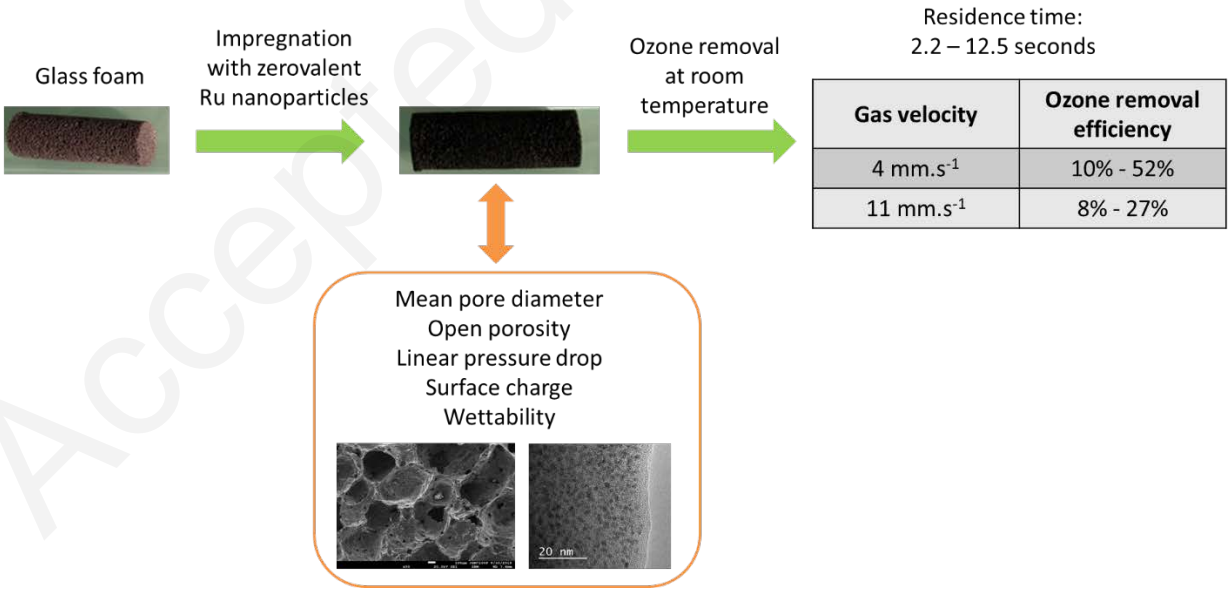

Introduction

Nowadays, heterogeneous catalysis is widely used in various fields such as fine chemistry, environment or petrochemistry. Actually, the use of catalysts allows to improve reaction efficiency and sometimes to work under softer operating conditions (temperature and pressure). Heterogeneous catalysts are generally preferred because they are easy to separate from the reaction mixture making their use widespread. They are usually composed of (i) a support that can be shaped with different geometries and (ii) a washcoat layer and then an active species deposited on the support (usually metals or metals oxides).

The most common supports are randomly packed catalyst pellets and structured catalysts [1-2]. Packed bed catalysts may contain catalyst particles such as zeolite pellets or granular activated carbon. They can have a very high surface area resulting in highly efficient reactions under kinetic control usually met in the chemical industry [3] and are less expensive than other catalytic materials [4]. Structured catalysts are usually ceramic (Al_2O_3, cordierite or SiC) or metallic (stainless steel, Al, Cu) materials [4]. Their pre-shaped structures are often monoliths honeycombs' matrix with many parallel channels of few millimeters' length. Their high void fraction combined with the laminar flow in the channels trigger low pressure drop and the well-defined regular geometry enables accurate predictive modelling of mass and heat transfer. However, both pellets and monoliths with parallel channels suffer from diffusional limitations as the turbulences are quite limited in this type of geometry. That is why for some years, the development of foams with open cells has known increased attention [5-6]. They are constituted of interconnected solid struts which enclosed cavities called pores [7-10] and are already used for thermal insulation and silencers. For catalytic processes, the advantages of this geometry, compared to the others above mentioned, come from better convection and radial dispersion lowering mass-transfer limitations. Metallic and ceramic foams are commercially available and can have high porosities combined with good mechanical strength and high surface area per unit volume. About process optimization and modelling, many studies deal with the characterization of metallic and ceramic foams, especially in terms of pressure drops, heat and mass transfers [11-15]. However, both ceramic and metallic foams are expensive (expensive raw material for metallic foams and high energy consumption for ceramic foam synthesis) and need a washcoat layer (usually γ-Al_2O_3) before impregnating the active species on the support [16,17]. Glass foams could be an efficient alternative to ceramic and metallic materials as their synthesis can be carried out in milder conditions (temperature around 700-900°C) and the raw materials are mainly recycled glass coming from wastes [18-20]. Glass foams are synthesized by a powder method with a mixture of broken glass and foaming agents (AlN, $CaCO_3$, SiC…). The mixture is heated at temperatures high enough to decompose the foaming agents which creates gases (N_2, CO_2, CO) that are trapped in the glass due to its low viscosity. The heat transfer and mechanical properties are quite good in these materials [19-21] and their properties can be modulated depending on the application targeted.

In our approach, the support material is impregnated with metal species active for the target reaction. Metal nanoparticles (NPs) have been considered with great interests because they offer good catalytic performances and selectivities owing to their original surface reactivities for several reactions such as hydrogenation, oxidation or Carbon-Carbon coupling reactions [22-24]. Moreover, their lifetime as well as resistance to poisoning can be improved depending on the type of metal and operating conditions used. They are often synthesized and stabilized in water allowing the potential of safe and soft impregnating conditions. For instance, metal NPs have already been deposited by the team on SiO_2 [25], TiO_2 [26] or magnetic supports [24,27].

This study aims to present the synthesis and demonstrate the catalytic activity of a patented material [28] composed of a glass foam impregnated with metal NPs. A set of glass foams was first prepared and characterized in terms of porosity, pore diameter, wettability, and linear pressure drops. Then, reduced ruthenium NPs were synthesized and impregnated on the support without washcoat layer. Such a catalyst could be used in gas or liquid phase and here for proof of efficiency, the impregnated glass foams were finally used for the removal of ozone from air at room temperature.

Experimental section

Material used for the characterizations

X-ray diffraction characterization conducted on crushed samples was realized at room temperature with a Philips PW3710 diffractometer operating with Cu Kα radiation (λ=1.5418 Å). The counting step and time were 0.02° and 1 second respectively. X'PERT softwares – Data Collector and Graphics and Identify – were used, respectively, for recording, analysis, and phase matching of the patterns.
A SurPass electrokinetic analyzer (Anton Paar Gmbh, Graz, Austria) equipped with a cylindrical cell was used to determine the zeta potential of glass foams from streaming potential measurements. All characterizations were carried out with a millimolar KCl solution.
Transmission Electron Microscopy (TEM, JEOL 2100) and Scanning Electron Microscopy (SEM, JEOL JSM 7100 F) were also performed on the synthesized materials.

Glass foam synthesis

In this study, crushed cullet from white glass bottles was used and crushed into powder. After sieving, 2 different granulometries were tested: (i) less than 100 µm and (ii) between 200 µm and 350 µm. The chemical glass composition was in weight percent: 73% SiO_2 – 1% Al_2O_3 – 15% Na_2O – 10% CaO. Three foaming and doping agents were used (i) aluminium nitride from H.C. Starck GmbH, (ii) titanium dioxide P25 from Hunstman Tioxide and (iii) manganese dioxide from Merck. The glass powder was mixed with the foaming and doping agents. Then, the thermal treatment of the mixtures was performed in a conventional electrical furnace (Nabertherm P300) up to 880°C. The heating rate was about 10 °C.min^{-1} and dwell temperature was maintained for 30 min to 1 hour. The cooling rate of the obtained foam material was governed by the furnace inertia.

Glass foam characterization

The glass foams were characterized by several techniques detailed below.

The apparent density ρ_{app} (kg.m^{-3}) was calculated with the ratio of the weight divided by the volume. The real sample density ρ_{real} (kg.m^{-3}) was determined with a helium pycnometer AccuPyc 1330 Micromeritics. Then, the open porosity ε (%) was calculated considering the real density and apparent one according to equation (1).

$$\varepsilon = \left(1 - \frac{\rho_{app}}{\rho_{real}}\right) \times 100 \quad (1)$$

The mean pore diameter d_p (mm) was determined from pictures of the cross section of the glass foams. The photos were treated and the contrast improved with ImageJ 1.52 software. Around one hundred pores were counted for each glass foam.

The specific surface area S ($m^2.m^{-3}$) was also determined but its calculation is not straightforward because it can significantly change depending on the pores geometry considered to do the calculation [11,15]. Richardson et al. [15] compared 3 models to determine the specific surface area of ceramic foams and advised the following formula depending on the mean pore diameter and the open porosity (equation (2)):

$$S = \frac{4 \times \varepsilon}{d_p \times (1 - \varepsilon)} \quad (2)$$

The wettability in water of the glass foams was characterized by a relative contact angle, calculated with the Washburn test [29]. The principle of the method was to measure the mass uptake of the material partly immersed in a liquid in function of time. It is carried out in (i) hexane (a reference solvent for which it is assumed that the contact angle is 0° because it has a low surface tension of around 19 $mN.m^{-1}$ at room temperature) and (ii) in water (the liquid of interest). Combining equations (3) and (4), which respectively deal with hexane and water, it was possible to calculate the contact angle between water and the glass foam.

$$1 = \frac{\Delta m^2 \times \eta_{hexane}}{\Delta t \times {\rho_{hexane}}^2 \times \gamma_{LV-hexane} \times C} \quad (3)$$

$$\cos \theta_{water} = \frac{\Delta m^2 \times \eta_{water}}{\Delta t \times {\rho_{water}}^2 \times \gamma_{LV-water} \times C} \quad (4)$$

With Δm the mass uptake (kg) during Δt time (s), η_{hexane} the hexane viscosity (Pa.s), ρ_{hexane} the hexane density ($kg.m^{-3}$), $\gamma_{LV-hexane}$ the surface tension between hexane and air ($N.m^{-1}$), C a constant to determine with equation (2), θ_{water} the surface angle between water and the glass foam (°), η_{water} the water viscosity (Pa.s), ρ_{water} the water density ($kg.m^{-3}$) and $\gamma_{LV-water}$ the surface tension between water and air ($N.m^{-1}$).

For one glass foam, the compressive strength was determined with a SHIMADZU Autograph AGS-X. The principle was to compress the glass foam at a speed of 1 $mm.min^{-1}$ and to measure the strength needed to reach such a compression. Five measurements were performed, and the average value was taken into account.

Finally, pressure drops measurements were performed with a "U" tube filled with water. The principle was to impose a gas feed flow controlled by a flow-meter (Brooks R-15-C) through the glass foam, inserted in a plastic tube, and calculating the pressure drops with the difference of the water height ΔH (m) in both sides of the "U" tube according to equation (5). The linear pressure drops (ratio of the pressure drops ΔP with the length of the glass foam L) were used to compare the different support synthesized.

$$\Delta P/L = [(\rho_{water} - \rho_{air}) \times \Delta H \times g]/L \quad (5)$$

With $\Delta P/L$ the linear pressure drops ($Pa.m^{-1}$) and ρ_{air} the air density ($kg.m^{-3}$). ρ_{air} was calculated at the working pressure and temperature through equation (5).

$$\rho_{air} = \frac{P \times MW}{R \times T} \quad (6)$$

With MW the molecular weight of air of 28.97 x 10^{-3} kg.mol^{-1}.

The float-type flow meter has been calibrated under controlled pressure and temperature. The read gas flow-rate ($Q_{G,read}$, L.h^{-1}) must be corrected taking into account pressure and temperature variability using equation (7):

$$Q_G(NL.h^{-1}) = Q_{G,read}(L.h^{-1}) \times \sqrt{\frac{P \times T_{calibration}}{P_{calibration} \times T}} \quad (7)$$

With Q_G the corrected gas flow-rate (NL.h^{-1}), P the pressure (Pa), $T_{calibration}$ the temperature during gas flow-meter calibration (K), $P_{calibration}$ the pressure during gas flow-meter calibration (Pa) and T the temperature (K). The prefix N stands for the Standard conditions of Temperature and Pressure (STP).

Nanoparticles synthesis and deposition on the glass foam

Zerovalent ruthenium nanoparticles (Ru(0)) were synthesized and characterized according to a methodology already published [30,31]. Briefly, ruthenium salt ($RuCl_3$, 3 H_2O) was solubilized in water. A mixture of surfactant (N,N-dimethyl-N-cetyl-N-(2-hydroxyethyl)ammonium chloride salt, HEA16Cl, lab-made, 2 equivalents) and reducing agent ($NaBH_4$, Acros Organics, 2.5 equivalents) was then added. The initial $RuCl_3$ concentration was 3.8 mM. The mixture was left 1 day at room temperature and atmospheric pressure under vigorous agitation to ensure complete salt reduction and an efficient stabilization by the ammonium salts. The surfactant avoids undesired agglomeration of NPs which have a size centered on 2.5 nm.
The glass foams were then impregnated by zerovalent ruthenium nanoparticles by simple immersion of the foam glass cylinder in the nanoparticles solution at room temperature and atmospheric pressure and finally dried in an oven at 100°C for several hours to remove water.

Ozone removal setup

Ozone removal in fixed bed catalytic glass foams was investigated with a continuous process (**Figure 1**) at room temperature (20 ± 2°C). A 40 L Tedlar® bag was filled at steady state with an oxygen/ozone mixture at an ozone concentration of 9 g.Nm^{-3}. This mixture was produced using an ozone generator (BMT 802, Germany). The ozone concentration of the mixture was measured using an on-line ozone analyzer (BMT 964, Germany). The gas mixture was pumped from the bag (KNF, Germany) to the process at a flow rate in the range 2.9-7.9 NL h^{-1}. A by-pass was used to control the initial ozone concentration and then, the reactor (glass foam impregnated with Ru(0) NPs) was fed and the outlet ozone concentration was quantified. The catalyst diameter was 16 mm and its length was around 60 mm depending on the sample. Thus, the gas velocity varied from 2.2 mm.s^{-1} to 12.5 mm.s^{-1} corresponding to gas hourly space velocity (GHSV) from 288 to 1636 h^{-1}. All experiments were carried out during at least 30 minutes in order to ensure steady-state conditions (no catalyst deactivation was observed).

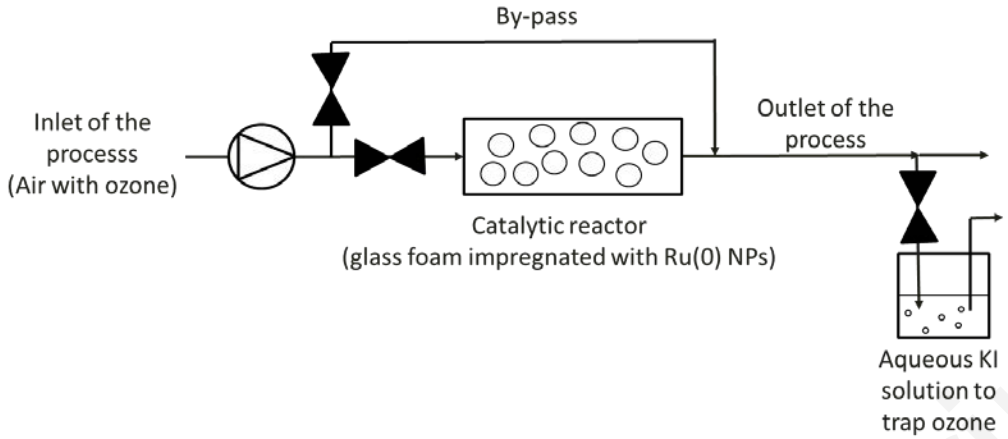

Figure 1. Layout of the setup for ozone removal at room temperature (20 ± 2°C) with glass foams impregnated with zerovalent ruthenium nanoparticles

Both the inlet and outlet ozone concentrations were quantified by the iodometric method. Basically, an absorber containing an iodide potassium aqueous solution was used to trap the ozone and sodium thiosulfate was further used to quantify the amount of iodine I_2 produced. The ozone concentration was deduced from the iodine concentration and the volume of gas analyzed.
The ozone removal efficiency (Eff, %) and reaction rate (R, $g.Nm^{-3}.s^{-1}$) were calculated according to equations (8) and (9), respectively.

$$Eff = \frac{[O_3]_{inlet} - [O_3]_{outlet}}{[O_3]_{inlet}} \times 100 \quad (8)$$

$$R = \frac{[O_3]_{inlet} - [O_3]_{outlet}}{\tau} \quad (9)$$

With $[O_3]_{inlet}$ the ozone concentration at the inlet of the reactor ($g.Nm^{-3}$), $[O_3]_{outlet}$ the ozone concentration at the outlet of the reactor ($g.Nm^{-3}$) and τ the residence time (s).

Results and discussions

Glass foam characterizations

General considerations

Eight different glass foams (not yet impregnated with NPs) were synthesized according to the methodology presented above. Their composition and the operating conditions (temperature and time of heating) are indicating in **Table 1**. Their real and apparent density as well as the open porosity ε, the contact angle and mean pore diameter d_p are also given in **Table 1**.
High open porosities were observed for the foams synthesized (between 73% and 92%) due to the fact that the foaming agent AlN decomposed under high temperature into Al_2O_3 and nitrogen according to equation (10). The formation of nitrogen gas bubbles gave this shape of foam when it escapes from the mixture.

$$2\ AlN(s) + 3\ O_2(g) \rightarrow 2\ Al_2O_3 + N_2(g) \quad (10)$$

The doping agents (TiO_2 and MnO_2) enhanced the foaming process according to equation (11) with TiO_2 as example [18].

$$3\ TiO_2(s) + 4\ AlN(s) \rightarrow 2\ Al_2O_3(s) + 3\ TiN(s) + 1/2\ N_2(g) \quad (11)$$

Moreover, MnO_2 can itself act as foaming agents. It can reduce into MnO or create Mn_2O_3, and release O_2 bubbles according to equations (12) and (13) [21].

$$2\ MnO_2(s) \rightarrow 2\ MnO(s) + O_2(g) \quad (12)$$

$$2\ MnO_2(s) \rightarrow Mn_2O_3(s) + 1/2\ O_2(g) \quad (13)$$

The X-ray diffractograms on **Figure 2** highlighted a partial devitrification as several peaks are observed. The crystallized phases identification with X'PERT software revealed the presence of numerous possible phases including mainly SiO_2 and a sodium and calcium silicate (JCPDS number for SiO_2: 01-077-1317 and JCPDS number for sodium and calcium silicate: 00-015-0690 and/or 00-023-0671). All X-ray diffractograms are not shown here as similar results were found. Only the relative intensity between crystalline and amorphous phases changed depending on the operating conditions and foam compositions used for the synthesis.

Figure 3 showed that all samples had a quite broad size distribution. They had monomodal distribution except Sample 5 which had a bimodal distribution. Bimodal distributions were already found by Østergaard et al. [32] for glass foams synthesized with various amounts of K_3PO_4. The maximum percentage of pores with same size ranged between 19% (Sample 3) and 45% (Sample 7). It seems that the higher the mean pore diameter, the narrower the pore size distribution. It has also to be highlighted that SEM pictures (**Figure 4**) confirmed the mean pore diameter determined from photo treatment with ImageJ software and given in **Table 1**.

The specific surface area was also estimated (**Table 1**) because it is an important parameter for the catalytic activity of the materials. It ranged between 5.3×10^4 $m^2.m^{-3}$ (21 $m^2.g_{foam}^{-1}$) and 18.0×10^4 $m^2.m^{-3}$ (61 $m^2.g_{foam}^{-1}$). Except for Samples 3 and 4, all the glass foams had high open porosity (around 90%) and so the specific surface area mainly depended on the mean pore diameter. The lower the mean pore diameter, the higher the specific surface area.

As explained in the experimental section, the calculation of the specific surface area significantly depends on geometrical considerations, that is why literature data were recalculated with equation (2) for sake of accurate comparison. Incera Garrido et al. [13] used various ceramic foams whose specific surface areas ranged between 0.9×10^4 $m^2.m^{-3}$ and 3.2×10^4 $m^2.m^{-3}$ and one stainless steel foam with a specific surface area of 11.2×10^4 $m^2.m^{-3}$. Richardson et al. [15] also worked with ceramic foams whose specific surface areas were between 1.7×10^4 $m^2.m^{-3}$ and 6.8×10^4 $m^2.m^{-3}$. These data highlighted that the glass foams here prepared had specific surface area in the upper range of available literature data. Furthermore, it has to be considered that the most important surface area regarding the catalyst activity might be due to the metal particles, not the support. Thus, owing to the low particle size of a few nanometers, a high surface area is expected.

The compressive strength was only determined for Sample 1 to give an order of magnitude for all the glass foams. Its compressive strength was 2.9 MPa. This value is in the range of experimental values of glass foam produced for insulation of buildings [19] which highlights the good mechanical resistance of the synthesized materials.

Table 1. Initial batch composition, process parameters, and characteristics of the foam samples prepared

Sample	Initial batch			Granulometry of the initial glass powder (µm)	T (°C)	Time (min)	Foam sample					
	AlN (wt.%)	TiO_2 (wt.%)	MnO_2 (wt.%)				ρ_{real} (g.cm^{-3})	ρ_{app} (g.cm^{-3})	Open porosity ε (%)	d_p (mm)	Contact angle (°)	S (10^{-4} m^2.m^{-3})
1	1.48	0.00	3.00	< 100	880	30	2.95	0.30	90	0.20	76	18.0
2	2.90	3.00	3.00	< 100	880	30	2.84	0.34	88	0.23	65	12.7
3	1.48	3.00	0.00	< 100	880	30	2.49	0.67	73	0.19	nd	5.7
4	0.60	1.16	1.16	< 100	880	30	2.63	0.59	77	0.11	47	12.2
5	0.60	4.84	4.84	< 100	880	30	3.50	0.26	92	0.43	76	10.7
6	0.60	4.84	4.84	< 100	850	30	2.40	0.22	91	0.50	nd	8.1
7	0.60	4.84	4.84	200 < X < 350	880	60	2.58	0.31	88	0.55	nd	5.3
8	0.60	4.84	4.84	< 100	850	60	2.12	0.23	89	0.51	nd	6.3

nd : not determined

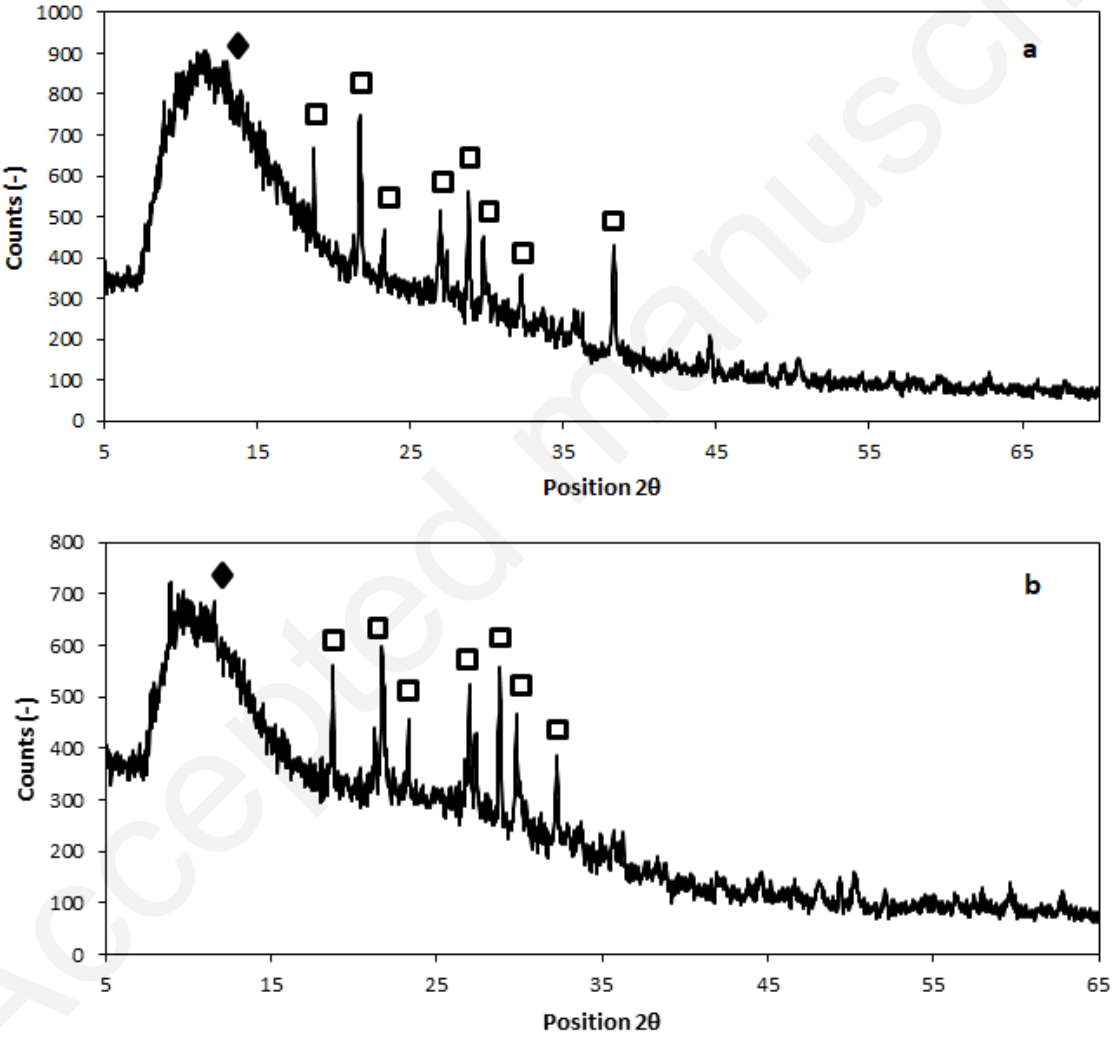

Figure 2. X-ray diffractograms of glass foams – a: Sample 5 – b: Sample 6 - □: sodium and calcium silicate (cristalline phase) - ♦: amorphous phase

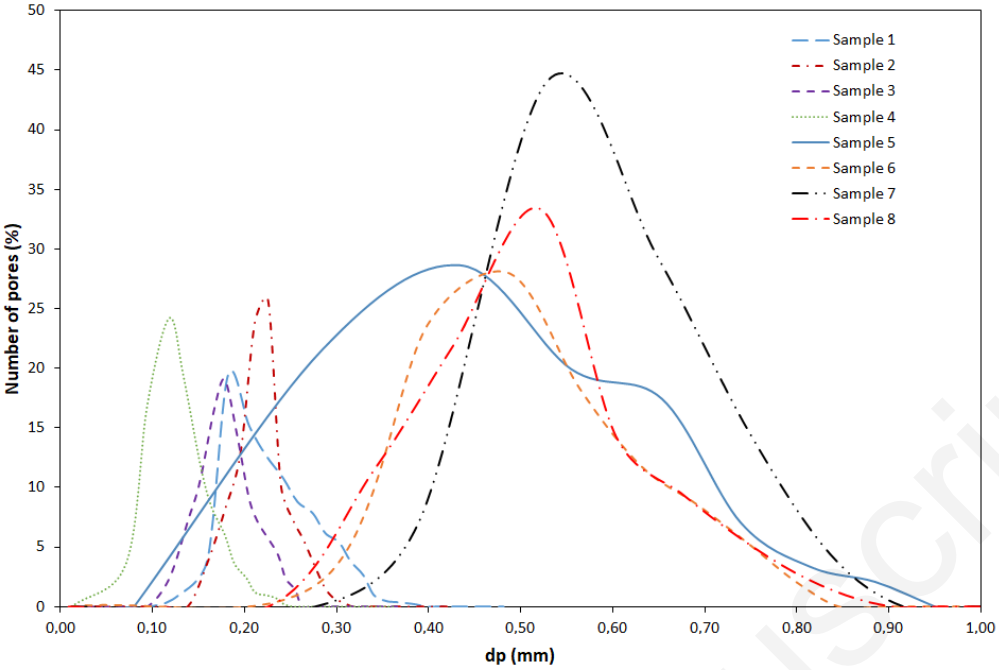

Figure 3. Distribution of pore size of glass foams

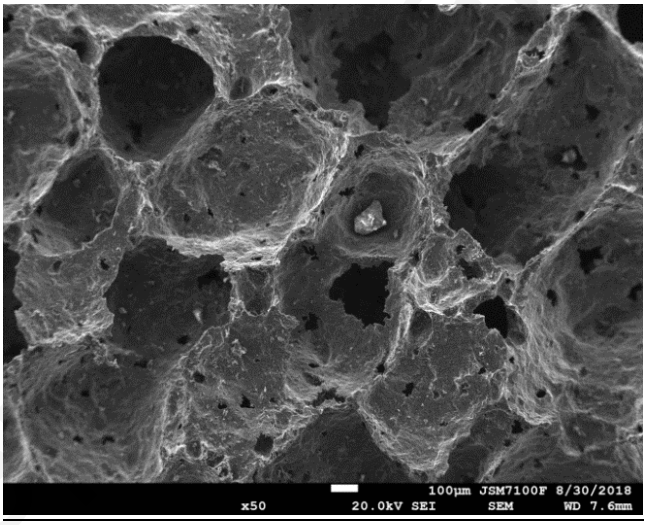

Figure 4. SEM picture of a glass foam

Detailed analysis of the characterizations

Samples 1 to 5 (**Table 1**) were prepared with the same conditions (T=880°C – 30 min – initial powdered glass granulometry lower than 100 µm) but varying the composition of the initial powder mixture.

Sample 3 was the only one without MnO_2 and it had the lowest open porosity reaching only 73% and a low mean pore diameter (0.19 mm). Sample 4 had the second lowest amount of MnO_2 (1.16 wt.%) among all the glass foam synthesized resulting in a low open porosity (77%) and mean pore diameter (0.11 mm). On the contrary, Sample 5 had the highest amount of MnO_2 (4.84 wt.%) and the biggest open porosity (92%) and big pores (0.43 mm),

highlighting the very positive effect of MnO_2 to reach highly open cell foam. Sample 5 had a large pore size distribution ranging from 0.08 mm to 0.95 mm.
Samples 1, 2 and 5 had almost the same open porosity (around 90%) but different mean pore diameters. Samples 1 and 2 had comparable mean pore diameters (0.20 and 0.23 mm, respectively) while sample 5 had bigger mean pore diameters (0.43 mm). According to these results, it seems that the higher the amount of MnO_2 and TiO_2, the bigger the pores, while it is not necessary to use more than 0.60% of AlN to get foam with large pores.
The contact angle was also an important parameter to deal with because the impregnation was performed in water solution (see Materials and method). The lower the contact angle, the better should be the ease of impregnation because the NPs in water should enter easier through the pores of the glass foam. The results are poorly correlated to the foam composition, Sample 4 had the lowest value (47°) while the other glass foams (Samples 1, 2 and 5) had contact angle between 65° and 76°. Anyway, these values, lower than 90°, highlight that the glass foams are hydrophilic, making the impregnation in water solution possible to perform.

Samples 5 to 8 had the same composition in foaming and doping agents (0.60% AlN, 4.84% TiO_2 and 4.84% MnO_2) but were prepared under different conditions (temperature and time of heating) and initial glass powder granulometry. This foam composition was selected because it has the biggest pores and open porosity among all tested initial batch compositions.
The temperature plays an important role in the formation of glass foam [33]. To investigate the effect of the temperature, samples were prepared for 30 min at 850°C and 880°C. The mean pore diameter of Sample 5 (880°C) was 0.43 mm and it was 0.50 mm for Sample 6 (850°C). It means that the average pore diameter decreased from 850°C to 880°C. This result agrees with Xi et al. [27] who observed a decrease of the pore size between 780°C and 790°C for glass ceramic foams made of titanium tailing. In fact, when the temperature increases, the viscosity of the raw material mixtures decreases, and the bubble are easier to expand [34,35]. However, at too high temperatures, the viscosity becomes too low and the pore structure is destroyed making the gas escapes and decreases the pore size. Moreover, another reason can explain this behavior. According to X-ray diffractograms of **Figure 2**, the intensity of the peaks of the crystal phase was higher at 880°C than at 850°C (compared to the intensity of the peak of the amorphous phase), meaning that the material was tougher and so the formation of big pores was more difficult to make. The apparent density followed the opposite trend than the mean pore size (it increased from 850°C to 880°C). The open porosity was almost the same at both temperatures which means that the links between the pores were fully achieved at 850°C.
To investigate the effect of the duration of heating, Sample 8 was also prepared at 850°C but heated for 60 min (against 30 min for all the others). Increasing the duration of heating did not significantly change the mean pore size (0.50 mm for 30 min and 0.51 mm for 60 min) nor the open porosity (91% for 30 min and 88% for 60 min) meaning that in this range of heating time and with this composition, a complete foaming process was achieved. Thus, to decrease energy consumption and save time for the process, it could be interesting to heat 30 min only.
Finally, the granulometry of the initial glass was increased to between 200 µm and 350 µm (Sample 7). This change did not improve the open porosity, but the mean pore size was the highest out of all glass foams (0.55 mm) and the narrowest size distribution among all glass foams synthesized (**Figure 3**).

Pressure drops measurements

Linear pressure drop measurements were also performed for each sample (**Figure 5**). This parameter is very important for industrial development as it is related to the energy consumption of the pump or fan to use. The aim is obviously to have a material with the lowest pressure drops. They were measured from around 0.025 $m.s^{-1}$ up to around 0.70 $m.s^{-1}$ (considering an empty tube) for the samples with the lowest pressure drops. The pressure drops increased with the gas superficial velocity in agreement with Darcy's law (**Figure 5**). Sample 4, which had the lowest mean pore diameter and second lowest open porosity, had the highest linear pressure drops among all tested glass foams. In contrary, Sample 7, which had the biggest mean pore diameter, had the lowest linear pressure drops values. These results mean that the higher the mean pore diameter and the open porosity, the lower the pressure drops. It agrees with current models used to describe pressure drops among foam materials [11-15]. According to the pore diameter and open porosity of the tested samples (**Table 1**), this tendency was always confirmed.

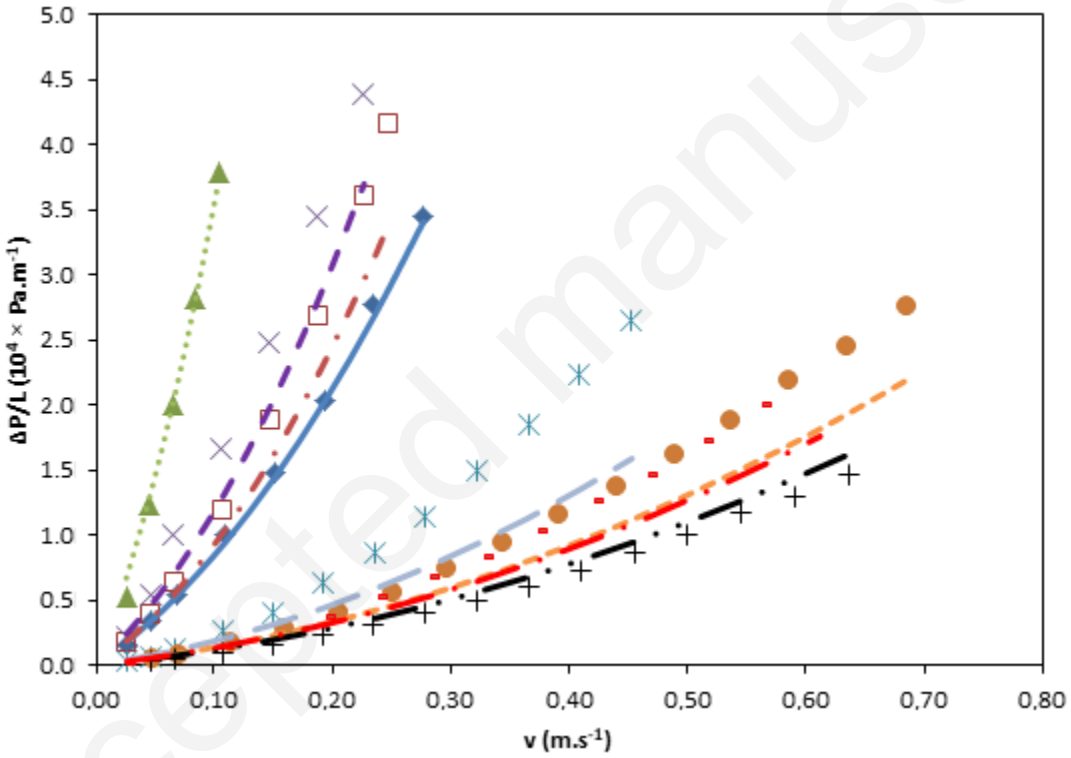

Figure 5. Experimental and modelled (equation (14)) linear pressure drops in function of the superficial gas velocity at 20°C for Samples 1-8: ♦: Sample 1 - □: Sample 2 - x: Sample 3 – ▲: Sample 4 - *-: Sample 5 - ●: Sample 6 - +: Sample 7 - -: Sample 8 – the full and dashed curves deal with the modelled data, the colors of the curves refers to the colors of the symbols

The pressure drops depend on the empty tube superficial gas velocity v ($m.s^{-1}$) and can be described with the Forchheimer equation successfully applied to ceramic foams (14) [36]. This latest depends on 2 parameters a_0 and a_1, which deals with inertial (viscous) and turbulent conditions, respectively [15,37]. Semi-empirical equations were here developed to model a_0 and a_1. According to the results explained above, they depend on the mean pore diameter and the open porosity (equations (15) and (16)).

$$\Delta P/L = a_0 \times v + a_1 \times v^2 \qquad (14)$$

$$a_0 = A \times {d_p}^{-B} \times (1-\varepsilon)^C \quad (15)$$

$$a_1 = A' \times {d_p}^{-B'} \times (1-\varepsilon)^{C'} \quad (16)$$

In equations (15) and (16), the 6 parameters (A, B, C, A', B', C') were fitted according to the experimental results (**Figure 5**). The results of modelling are presented in **Table 2**. Accurate fitting was found with less than 30% of average error on the linear pressure drop for the 8 samples, and less than 20% of average error for 6 samples out of 8 although the pressure drop can vary by two orders of magnitude at a given value of v depending on the sample (**Figure 4**).

Table 2. Fitted parameters to describe the pressure drops in function of the superficial gas velocity with equation 13 for the 8 glass foam samples - $A=4.1\times10^4$ - B=1.9 - C=0.2 - $A'=6.0\times10^4$ - B'=2.4 - $C'=6.0\times10^{-3}$

Sample	a_0 experiment	a_1 experiment	a_0 model	a_1 model	Average error on the linear pressure drop (%)
1	6.4×10^5	2.2×10^6	6.2×10^5	3.0×10^6	4.6
2	6.7×10^5	4.0×10^6	5.0×10^5	2.2×10^6	14.5
3	1.2×10^6	3.4×10^6	8.2×10^5	3.6×10^6	19.3
4	1.8×10^6	1.8×10^7	2.2×10^6	1.3×10^7	7.6
5	1.2×10^5	1.0×10^6	1.4×10^5	4.7×10^5	29.0
6	1.3×10^5	4.1×10^5	1.0×10^5	3.2×10^5	18.9
7	7.4×10^4	2.5×10^5	9.2×10^4	2.6×10^5	19.5
8	1.1×10^5	2.5×10^5	1.0×10^5	3.0×10^5	25.1

The good agreement between the experimental and the theoretical values is not a sufficient condition to confirm the accuracy of the parameters determined previously and the robustness of the model. Indeed, each parameter has a variable influence on the linear pressure drops. This influence can be assessed through a sensitivity analysis based on the elasticity index determination. It addresses the relative significance of potential errors in various input parameters [38,39]. The elasticity index EI measures the relative change of the parameters a_0 and a_1 for a relative change in an input parameter (open porosity ε or mean pore diameter d_p), as shown in equation (17) for a_0 with the open porosity and a relative change of 5% (the same equation was applied to a_1).

$$EI = \frac{\varepsilon}{a_0} \times \frac{1}{2} \times \left(\frac{a_{0+5\%} - a_0}{\varepsilon_{+5\%} - \varepsilon} + \frac{a_{0-5\%} - a_0}{\varepsilon_{-5\%} - \varepsilon} \right) \quad (17)$$

The values of the elasticity index are given in **Table 3**. The average EI values are quite low whatsoever for the input parameter d_p or ε which strengthens the accuracy of the model.

Table 3. Elasticity index (EI) determination for a_0 and a_1 for a relative change of 5%

Parameter a_0		
Input parameter	Open porosity ε	Mean pore diameter d_p
Average EI (-)	-0.41	-0.25
Parameter a_1		
Input parameter	Open porosity ε	Mean pore diameter d_p
Average EI (-)	0.12	-0.01

Other parameters such as the pore size distribution or the tortuosity may also play a crucial role in pressure drop measurements. Sometimes, the shape of the strut between the pores is also taken into account in the model for geometrical considerations [14]. Here, the glass foams have triangle struts according to the SEM pictures (**Fig. 4)**.
For Sample 7, at low gas velocity where the second term of equation (14) dealing with the square of the gas velocity is almost negligible (the term $a_0 \times v$ is 10 times higher than the term $a_1 \times v^2$ until a gas velocity of 0.03 $m.s^{-1}$ for Sample 7), the measured pressure drops are comparable with the pressure drops of commercial ceramic and metallic foams [13,15]. However, at higher gas velocities, the best available ceramic and metallic foams have lower pressure drops.

According to these results, Sample 7 showed the lowest pressure drop that is why this support will be further detailed for NPs impregnation and ozone decomposition.

Characterization of zerovalent ruthenium nanoparticles deposited on the glass foam

In a first step, zerovalent ruthenium NPs (part 2.4) were prepared in water and were impregnated on glass foams according to the wet methodology. First of all, after impregnation, the glass foam surface color changed from purple to black. This black color is typical of the reduced Ru nanospecies that were deposited on the support. The linear pressure drops and open porosity were also measured after impregnation and there was no significant difference compared to the virgin glass foam.

In order to characterize the deposit of Ru(0) NPs on the glass foam, streaming potential measurements were carried out on a virgin glass foam and an impregnated one, both filled with an electrolyte solution (10^{-3} $mol.L^{-1}$ KCl) (**Figure 6**). The principle was to apply a pressure gradient through the glass foam that developed a surface charge in contact with the electrolyte solution. The charges in the mobile part of the electrical double layer were carried toward the low pressure-side resulting in a steady-state electric potential difference (the streaming potential) [40] that was measured through the glass foam by means of two Ag/AgCl electrodes placed on both sides of the porous medium. The zeta potential was further determined by the well-known Helmholtz-Smoluchowski equation since the pore size was much larger than the Debye length of the measuring solution (~10 nm) [41]. The impregnation of Ru(0) NPs had two consequences on the surface charge: (i) the isoelectric point (pH for which the effective surface charge is null) moves from 2.3 for a virgin glass foam (in agreement with literature data of glass measurement [42,43]) to 3.0 for the impregnated one, (ii) the impregnated foam has a lower negative charge (zeta potential less than -10 mV) compared to the virgin one (zeta potential of -20 mV at the most). Surfactant stabilized Ru(0) NPs are positively charged [44] which means that the increase of the material charge is due to the successful deposit of the NPs on the support. The same results were found with all the tested glass foams.
Finally, TEM experiments were investigated to locate Ru(0) NPs on the glass foam (**Figure 7**). Nanoparticles were well dispersed on the support due to the prior stabilization of species in the aqueous solution before the deposit. Spherical and isolated nanoparticles were observed with an average diameter about of 2.5 nm. The treatment of the TEM images (with ImageJ 1.52 software) permitted to determine that around 23% of the glass foam surface was doped with ruthenium nanoparticles

The leaching of the NPs deposited on the glass foam which could be a major drawback to the use of the catalyst, was considered. As the catalyst can be used both for liquid and gas

applications, the leaching was first assessed with a Soxhlet apparatus with water (heated at 150°C for 4h) and then after long-term exposition to air flow (0.4 $m.s^{-1}$ during 72h, representing 21 m^3 of air that passed through the catalyst and that was trapped in water for Ru quantification). Both solutions were analyzed with inductive coupled plasma-optical emission spectrometry to determine the Ru concentration. At the end of the experiments, only 0.05 ppm of ruthenium was found in water from Soxhlet and the air content in ruthenium was 2×10^{-5} ppm, showing in both cases the extremely low release of NPs.

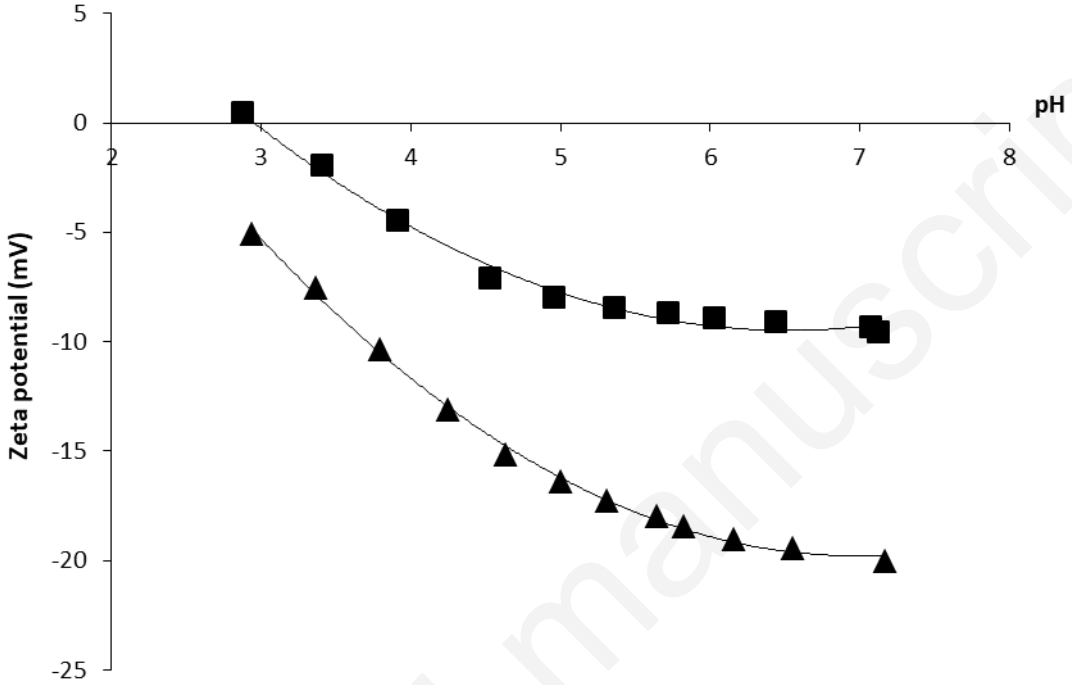

Figure 6. pH dependence of the zeta potential (determined with millimolar KCl solution): ▲: virgin glass foam - ■: glass foam impregnated with zerovalent ruthenium nanoparticles

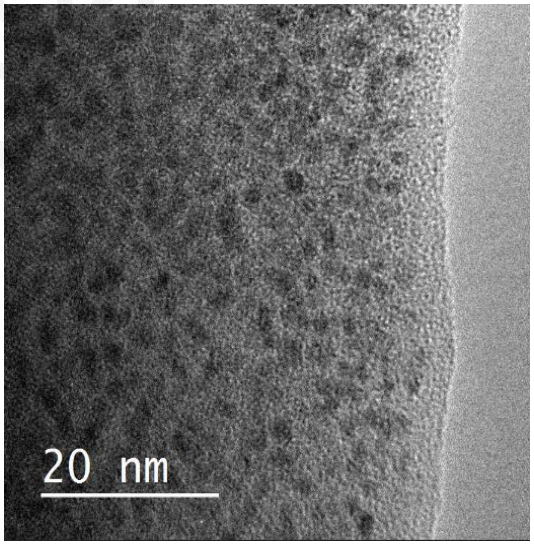

Figure 7. TEM picture of zerovalent ruthenium nanoparticles deposited on a glass foam

Ozone removal

Sample 7, synthesized with a granulometry of the initial glass powder between 200 µm and 350 µm, was impregnated with zerovalent ruthenium nanoparticles and used for ozone removal. The process was carried out in the air, at room temperature, at an inlet concentration of 9 $g.m^{-3}$ and at two different gas velocities.
As explained above, the composition of Sample 7 permitted to get the lowest pressure drop, making this glass foam the best choice for lowering energy consumption. Nevertheless, two other glass foams were also synthesized with the same operating conditions (**Table 1**) and the same glass granulometry in order to see the influence of the catalyst characteristics. These samples, named 9 and 10, had the following composition and main characteristics:

- Sample 9: 1.48% AlN, 0.00% TiO_2 and 3.00 % MnO_2, 84% of open porosity and 0.47 mm of mean pore size
- Sample 10: 0.60% AlN, 1.16% TiO_2 and 1.16 % MnO_2, 73% of open porosity and 0.32 mm of mean pore size

According to their open porosity and mean pore diameter, samples 9 and 10 clearly engender higher pressure drops than Sample 7.

First, we have checked that a glass foam not impregnated with ruthenium nanoparticles did not show any activity for ozone removal from air.
The results about ozone decomposition at room temperature are summed up in **Table 4**. Whatsoever the glass foam, the ozone abatement decreased with an increase in the gas velocity. For instance for Sample 7, at 4 $mm.s^{-1}$, the ozone abatement was 31% and decreased to 23% at 11 $mm.s^{-1}$ for a residence time around three times lower. These removal efficiencies, which can be considered as moderate, were nonetheless gathered using high ozone inlet concentrations and leads to a high reaction rate from 0.2 to more than 0.6 g Nm^{-3} s^{-1}. These results demonstrate that the reaction rate was two times higher at 11 $mm.s^{-1}$ highlighting that in this range of gas speed, the external mass transfer is still limiting the process performances. In this range of gas flow, the Reynolds number is lower than 1 (the calculation was done considering the gas velocity of the empty tube and the pore diameter [9]), meaning that flow is clearly laminar which does not promote efficient mass transfer. Thus, at higher superficial velocities and similar residence time, higher ozone removal efficiencies will be reached.
Ozone was already removed from air with several types of catalysts [45]. Very high removals were found with metal oxide on cordierite foams for instance but the ozone concentrations were generally low (around 1-10 ppm) making the comparison with our results difficult. As mentioned in the literature for other types of catalysts [46], ozone may decompose to O_2 on the active ruthenium sites at the catalyst surface and may form oxygen active species that could also be used on a second step for oxidation reaction. Actually, some works focused on the removal of volatile organic compounds in air by catalytic ozonation [47,48]. This process can also be used in water treatment [49,50] for the removal of pharmaceuticals that could be another application of the catalytic glass foams here prepared.

Comparing the results with the three glass foams, Sample 9 had the highest reaction rate followed by Sample 7 and finally Sample 10. According to these results, the activity does not seem to be linked with the characteristics (open porosity and mean pore size) of the catalysts. Therefore, Sample 10 seems to be the least interesting catalyst because it had the lowest reaction rate as well as the highest pressure drop. However, a compromise needs to be found between Sample 7 and 9. On the one hand, Sample 7 had the lowest pressure drop but on the

other hand, Sample 9 was the most active catalyst. Anyway, these experiments confirmed the catalytic activity of the developed materials.

Table 4. Performances of 3 different glass foams impregnated with Ru(0) NPs for the removal of ozone from air (T=20±2°C ; $[O_3]_{inlet}$=9 g.m^{-3})

Sample	Gas velocity (mm.s^{-1})	Residence time (s)	Eff (%)	R (g.Nm^{-3}.s^{-1})
7	4	12.5	31	0.23
	11	4.7	23	0.46
9	4	10.7	52	0.37
	11	4.0	27	0.66
10	4	5.9	10	0.19
	11	2.2	8	0.38

Conclusion

The synthesis and characterization of a recently patented heterogeneous catalyst was shown. It first consists of an open-cell support called glass foam whose open porosity and mean pore diameter can be tuned depending on the quantity of foaming and doping agents, the initial glass powder granulometry as well as the temperature and time of heating. It was clearly highlighted a positive effect of MnO_2 and TiO_2 to increase both the open porosity and the mean pore diameter. Pressure drops measurements showed, in agreement with literature data, that the highest the open porosity and the mean pore diameter, the lowest the pressure drops. An optimal composition and operating conditions were so found to get the glass foam with the lowest pressure drops. The second step of the catalyst synthesis deals with the wet impregnation of an aqueous suspension of pre-stabilized zerovalent Ru nanoparticles (aiming to 0.1 wt.%) using a mild methodology by immersion in a water solution at room temperature and pressure and drying to remove water. Zeta potential measurements and TEM images highlighted the successful deposit of the NPs on the glass foam, and TEM images showed that NPs are well dispersed with an average diameter of about 2-3 nm. Finally, the catalyst was tested for ozone removal in the air at room temperature for proof of activity. With the glass foam with the lowest pressure drops, between 23% and 31% of ozone removal efficiency was observed depending on the gas flow at ambient temperature and it was highlighted that the performances would be significantly better by increasing the gas velocity to overcome mass transfer limitations. High reaction rate were achieved despite the low temperature applied and significant improvements will be expected with an increase in the temperature.

Acknowledgments

The authors thank the SATT Ouest Valorisation for financial support. The authors also thank Vincent Dorcet for TEM analyses, Loïc Joanny for SEM analyses (ScanMAT - UMS 2001) and Bertrand Lefeuvre for ICP-OES analyses.

References

(1) García-Bordejé, E.; Liu, Y.; Su, D.S.; Pham-Huu, C. Hierarchically structured reactors containing nanocarbons for intensification of chemical reactions, J. Mat. Chem. A. 5 (2017) 22408-22441.

(2) Pangarkar, K.; Schildhauer, TJ.; Ruud van Ommen, J.; Nijenhuis, J.; Kapteijn, F.; Moulijn, J. Structured Packings for Multiphase Catalytic Reactors, Ind. Eng. Chem. Res. 47 (2008) 3720-3751.

(3) Levenspiel, O. Chemical Engineering design - Third Edition, Wiley (1999).

(4) Tronconi, E.; Groppi, G.; Visconti, C.G. Structured catalysts for non-adiabatic applications, Curr. Opin. Chem. Eng. 5 (2014) 55–67. doi:10.1016/j.coche.2014.04.003.

(5) Balkanli, E.; Figen, H.E. Sodium borohydride hydrolysis by using ceramic foam supported bimetallic and trimetallic catalysts, Int. J. Hydrog. Energy. 44 (2019) 9959–9969. doi:10.1016/j.ijhydene.2018.12.010.

(6) Gao, N.; Han, Y.; Quan, C. Study on steam reforming of coal tar over NiCo/ceramic foam catalyst for hydrogen production: Effect of Ni/Co ratio, Int. J. Hydrog. Energy. 43 (2018) 22170–22186. doi:10.1016/j.ijhydene.2018.10.119.

(7) Luyten, J.; Mullens, S.; Cooymans, J.; De Wilde, A. M.; Thijs, I.; Kemps, R. Different methods to synthesize ceramic foams, J. Eur. Ceram. Soc. 29 (2009) 829-832.

(8) Dhara, S.; Bhagarva, P. A simple direct casting route to ceramic foams, J. Am. Ceram. Soc. 86 (2003) 1645-1650.

(9) Han, X.; Wang, Q.; Park, Y-G.; T'Joen, C.; Sommers A.; Jacobi, A. A Review of Metal Foam and Metal Matrix Composites for Heat Exchangers and Heat Sinks, Heat Transf. Eng. 33 (2012)

(10) Park, C.; Nutt, S.R. Effects of process parameters on steel foam synthesis, Mat. Sci. Eng. A, 297 (2001) 62-68.

(11) Groppi, G.; Giani, L.; Tronconi, E. Generalized Correlation for Gas/Solid Mass-Transfer Coefficients in Metallic and Ceramic Foams, Ind. Eng. Chem. Res. 46 (2007) 3955–3958. doi:10.1021/ie061330g.

(12) Bracconi, M.; Ambrosetti, M.; Maestri, M.; Groppi, G.; Tronconi, E. A fundamental investigation of gas/solid mass transfer in open-cell foams using a combined experimental and CFD approach, Chem. Eng. J. 352 (2018) 558–571. doi:10.1016/j.cej.2018.07.023.

(13) Incera Garrido, G.; Patcas, F.C.; Lang, S.; Kraushaar-Czarnetzki, B. Mass transfer and pressure drop in ceramic foams: A description for different pore sizes and porosities, Chem. Eng. Sci. 63 (2008) 5202–5217. doi:10.1016/j.ces.2008.06.015.

(14) Lucci, F.; Della Torre, A.; Von Rickenbach, J.; Montenegro, G.; Poulikakos, D.; Dimopoulos Eggenschwiler, P. Performance of randomized Kelvin cell structures as catalytic substrates: Mass-transfer based analysis, Chem. Eng. Sci. 112 (2014) 143–151. doi:10.1016/j.ces.2014.03.023.

(15) Richardson, J.T.; Peng, Y.; Remue, D. Properties of ceramic foam catalyst supports: pressure drop, Appl. Catal. Gen. 204 (2000) 19–32. doi:10.1016/S0926-860X(00)00508-1.

(16) Giani, L.; Cristiani, C.; Groppi, G.; Tronconi, E. Washcoating method for Pd/γ-Al2O3 deposition on metallic foams, Appl. Catal. B Environ. 62 (2006) 121–131. doi:10.1016/j.apcatb.2005.07.003.

(17) Zhang, H.; Suszynski, W.J.; Agrawal, K.V.; Tsapatsis, M.; Al Hashimi, S.; Francis, L.F. Coating of Open Cell Foams, Ind. Eng. Chem. Res. 51 (2012) 9250–9259. doi:10.1021/ie300266p.

(18) Lebullenger, R.; Chenu, S.; Rocherullé, J.; Merdrignac-Conanec, O.; Cheviré, F.; Tessier, F.; Bouzaza, A.; Brosillon, S. Glass foams for environmental applications, J. Non-Cryst. Solids. 356 (2010) 2562–2568. doi:10.1016/j.jnoncrysol.2010.04.050.
(19) König, J.; Petersen, R.R.; Yue, Y. Influence of the glass particle size on the foaming process and physical characteristics of foam glasses, J. Non-Cryst. Solids. 447 (2016) 190–197. doi:10.1016/j.jnoncrysol.2016.05.021.
(20) Hrma, P. Effect of heating rate on glass foaming: Transition to bulk foam, J. Non-Cryst. Solids. 355 (2009) 257–263. doi:10.1016/j.jnoncrysol.2008.11.007.
(21) Petersen, R.R.; König, J.; Yue, Y. The mechanism of foaming and thermal conductivity of glasses foamed with MnO2, J. Non-Cryst. Solids. 425 (2015) 74–82. doi:10.1016/j.jnoncrysol.2015.05.030.
(22) Serp, P.; Philippot, K. Nanomaterials in Catalysis, Wiley-VCH, Weinheim, (2013) 496 pp.
(23) Polshettiwar, V.; Asefa, T. Nanocatalysis: Synthesis and Applications, Wiley (2013) 736 pp.
(24) Denicourt-Nowicki, A.; Roucoux, A. Odyssey in Polyphasic Catalysis by Metal Nanoparticles, The Chemical Record, 16 (2016) 2127-2141.
(25) Mévellec, V.; Nowicki, A.; Roucoux, A.; Dujardin, C.; Granger, P.; Payen, E.; Philippot, K. A simple and reproducible method for the synthesis of silica-supported rhodium nanoparticles and their investigation in the hydrogenation of aromatic compounds, New J. Chem. 30 (2006) 1214–1219. doi:10.1039/B605893K.
(26) Hubert, C.; Bilé, E.G.; Denicourt-Nowicki, A.; Roucoux, A. Rh(0) colloids supported on TiO2: a highly active and pertinent tandem in neat water for the hydrogenation of aromatics, Green Chem. 13 (2011) 1766–1771. doi:10.1039/C0GC00931H.
(27) Pélisson, C.-H.; Denicourt-Nowicki, A.; Roucoux, A. Magnetically Retrievable Rh(0) Nanocomposite as Relevant Catalyst for Mild Hydrogenation of Functionalized Arenes in Water, ACS Sustain. Chem. Eng. 4 (2016) 1834–1839. doi:10.1021/acssuschemeng.6b00045.
(28) Biard, P.-F.; Couvert, A.; Denicourt, A.; Roucoux, A.; Lebullenger, R. Nanoparticules métalliques supportées sur un support en mousse de verre et utilisations pour la catalyse de réactions chimiques, WO2017064418A1, 2017.
(29) Wettability studies for porous solids including powders and fibrous materials, KRUSS GmbH technical note.
(30) Nowicki, A.; Boulaire, V.L.; Roucoux, A. Nanoheterogeneous Catalytic Hydrogenation of Arenes: Evaluation of the Surfactant-Stabilized Aqueous Ruthenium(0) Colloidal Suspension, Adv. Synth. Catal. 349 (2007) 2326–2330. doi:10.1002/adsc.200700208.
(31) Lebedeva, A.; Albuquerque, B.L.; Domingos, J.B.; Lamonier, J.-F.; Giraudon, J.-M.; Lecante, P.; Denicourt-Nowicki, A.; Roucoux, A. Ruthenium Trichloride Catalyst in Water: Ru Colloids versus Ru Dimer Characterization Investigations, Inorg. Chem. 58 (2019) 4141–4151. doi:10.1021/acs.inorgchem.8b03144.
(32) Østergaard, M.B.; Cai, B.; Petersen, R.R; König, J.; Lee, P.D.; Yue, Y. Impact of pore structure on the thermal conductivity of glass foams, Mater. Lett. 250 (2019) 72-74.
(33) Llaudis, A.S.; Tari, M.J.O.; Ten, F.J.G.; Bernardo, E.; Colombo, P. Foaming of flat glass cullet using Si3N4 and MnO2 powders, Ceram. Int. 35 (2009) 1953–1959. doi:10.1016/j.ceramint.2008.10.022.
(34) Xi, C.; Zheng, F.; Xu, J.; Yang, W.; Peng, Y.; Li, Y.; Li, P.; Zhen, Q.; Bashir, S.; Liu, J.L. Preparation of glass-ceramic foams using extracted titanium tailing and glass waste as raw materials, Constr. Build. Mater. 190 (2018) 896–909. doi:10.1016/j.conbuildmat.2018.09.170.

(35) König, J.; Petersen, R.R.; Yue, Y. Influence of the glass–calcium carbonate mixture's characteristics on the foaming process and the properties of the foam glass, J. Eur. Ceram. Soc. 34 (2014) 1591–1598. doi:10.1016/j.jeurceramsoc.2013.12.020.
(36) Forchheimer, P.H. Wasserbewegung durch Boden, Zeitschrift des Vereins deutscher Ingenieure, Düsseldorf, 1901.
(37) Ergun, S.; Orning, A.A. Fluid Flow through Randomly Packed Columns and Fluidized Beds, Ind & Eng Chem.41 (1949) 1179-1184.
(38) Vilmain, J.-B.; Courousse, V.; Biard, P.-F.; Azizi, M.; Couvert, A. Kinetic study of hydrogen sulfide absorption in aqueous chlorine solution, Chem. Eng. Res. Des. 92 (2014) 191–204. doi:10.1016/j.cherd.2013.07.015.
(39) Yin, H.; Wu, S.; Ejeta, M. California, Department of Water Resources, Bay-Delta Office, CalSim-II model sensitivity analysis study: technical memorandum report, Department of Water Resources, Bay-Delta Office, Sacramento, Calif., 2005.
(40) Szymczyk, A.; Labbez, C.; Fievet, P.; Aoubiza, B.; Simon, C. Streaming potential through multilayer membranes, AIChE J. 47 (2001) 2349–2358. doi:10.1002/aic.690471019.
(41) Sbaï, M.; Fievet, P.; Szymczyk, A.; Aoubiza, B.; Vidonne, A.; Foissy, A. Streaming potential, electroviscous effect, pore conductivity and membrane potential for the determination of the surface potential of a ceramic ultrafiltration membrane, J. Membr. Sci. 215 (2003) 1–9. doi:10.1016/S0376-7388(02)00553-7.
(42) Andrade, A.L.; Souza, D.M.; Pereira, M.C.; Fabris, J.D.; Domingues, R.Z. Síntese e caracterização de nanopartículas magnéticas revestidas com sílica através de um processo sol-gel, Cerâmica. 55 (2009) 420–424. doi:10.1590/S0366-69132009000400013.
(43) Lameiras, F.S.; de Souza, A.L.; de Melo, V.A.R.; Nunes, E.H.M.; Braga, I.D. Measurement of the zeta potential of planar surfaces with a rotating disk, Mater. Res. 11 (2008) 217–219. doi:10.1590/S1516-14392008000200018.
(44) Bilé, E.G.; Sassine, R.; Denicourt-Nowicki, A.; Launay, F.; Roucoux, A. New ammonium surfactant-stabilized rhodium(0) colloidal suspensions: Influence of novel counter-anions on physico-chemical and catalytic properties, Dalton Trans. 40 (2011) 6524–6531. doi:10.1039/C0DT01763A.
(45) Dhandapani, B.; Oyama, S.T. Gas phase ozone decomposition catalysts, Appl. Cat. B: Env. 11 (1997) 129-166
(46) Radhakrishnan, R.; Oyama, S.T.; Ohminami, Y.; Asakura, K. Structure of MnOx/Al2O3 Catalyst: A Study Using EXAFS, In Situ Laser Raman Spectroscopy and ab Initio Calculations, J. Phys. Chem. B. 105 (2001) 9067–9070. doi:10.1021/jp004480s.
(47) Einaga, H.; Futamura, S. Oxidation behavior of cyclohexane on alumina-supported manganese oxides with ozone, Appl. Cat B: Env. 60 (2005) 49-55.
(48) Wang, H.C.; Chang, S.H.; Hung, P.C.; Hwang, J.F.; Chang, M.B. Catalytic oxidation of gaseous PCDD/Fs with ozone over iron oxide catalysts, Chemosphere, 71 (2008) 388-397.
(49) Restivo, J.; Órfão, J. J. M.; Pereira, M. F. R.; Vanhaecke, E.; Rönning, M.;. Iouranova, T.; Kiwi-Minsker, L.; Armenise, S.; Garcia-Bordejé, E. Catalytic ozonation of oxalic acid using carbon nanofibres on macrostructured supports, Water Sci Technol (2012) 65 (10) 1854-1862.
(50) Yang, L.; Hu, C.; Nie, Y.; Qu, J. Catalytic Ozonation of Selected Pharmaceuticals over Mesoporous Alumina-Supported Manganese Oxide, Environ. Sci. Technol. 43 (2009) 2525-2529.

For Table of Contents Use Only

Table of contents graphic

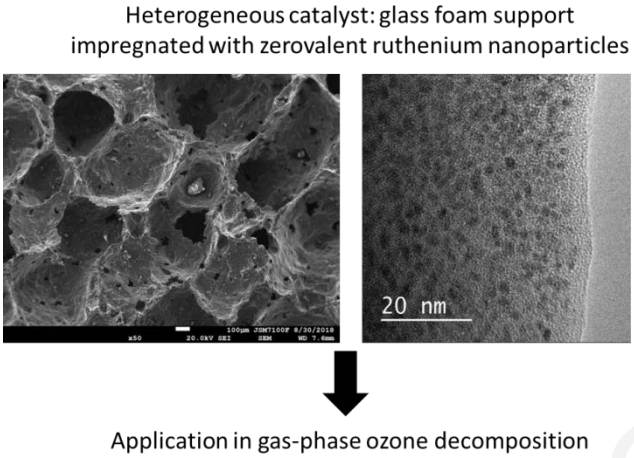

Synopsis

Heterogeneous catalysts, composed of an open-cell glass foam support impregnated with zerovalent ruthenium nanoparticles, were synthesized, characterized and used for ozone removal from air.